JOURNAL OF
APPLIED
CRYSTALLOGRAPHY

Volume 53 (2020)

Supporting information for article:

DLSR: A solution to the parallax artefact in X-ray diffraction computed tomography data

Antonis Vamvakeros, Alan A. Coelho, Dorota Matras, Hongyang Dong, Yaroslav Odarchenko, S. W. T. Price, K. T. Butler, O. Gutowski, A.-C. Dippel, M. Zimmermann, I. Martens, J. Drnec, A. M. Beale and S. D. M. Jacques

S1. Experimental setup at P07, DESY

Photographs of the experimental setup used for the parallax XRD-CT measurements performed at beamline station P07 (EH2) at PETRA III, DESY, are presented in Figure S1. The 3D printed sample holder was mounted directly onto the rotation stage which was mounted perpendicular to the hexapod. The hexapod facilitated the various translation movements (i.e. along and across the beam).

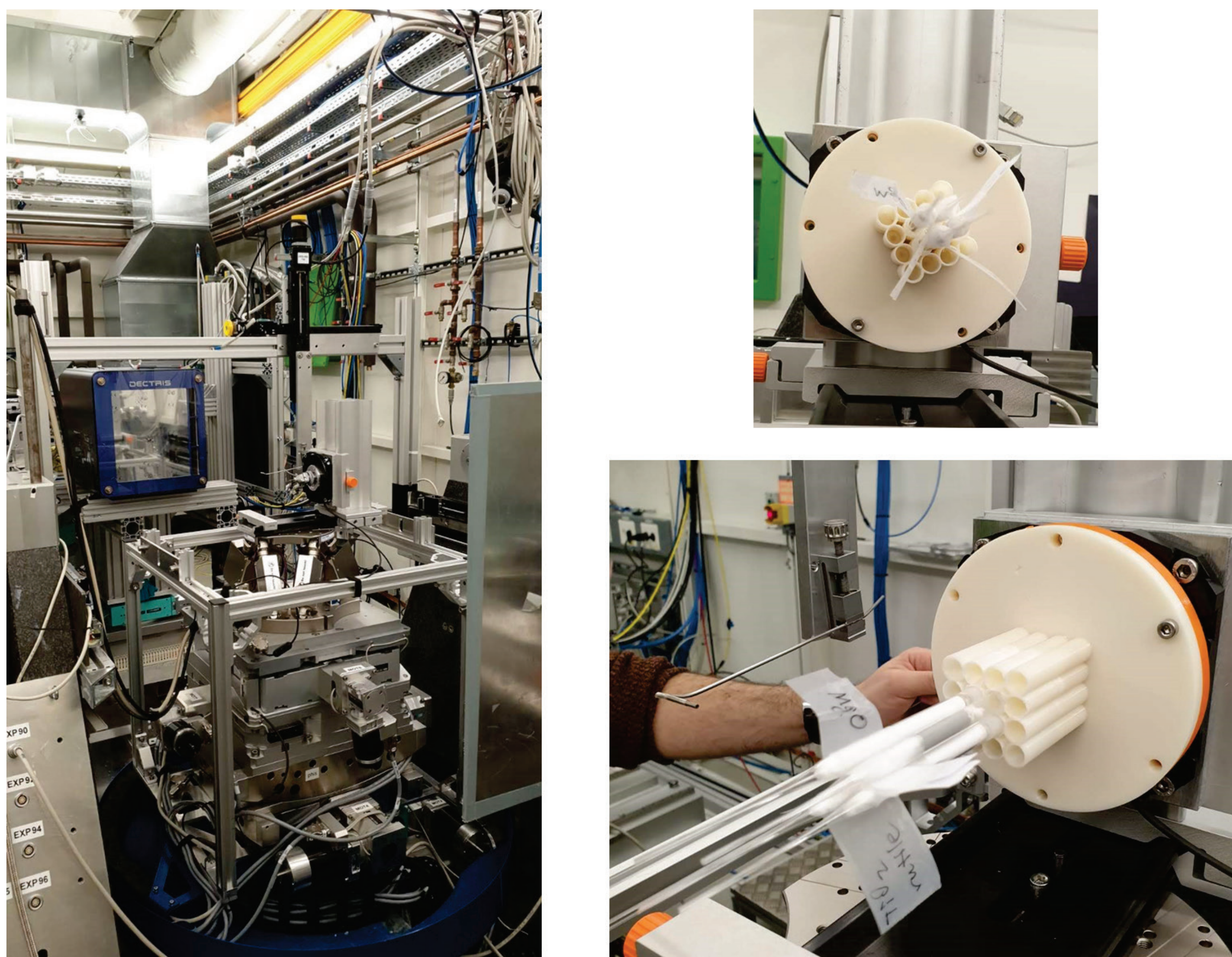

Figure S1: Photographs of the experimental setup used at beamline station P07 (EH2) at PETRA III, DESY

The sample holder for the phantom object was 3D printed from the ABS plastic using the Stratasys F170 printer. The holder consisted of a 4 × 4 array of semi hollow cylinders with outer diameter of 9 mm designed to hold the glass pipettes filled with the powder samples. The dimensions of

the holder are 120x120x58 mm^3 and the printing took ca. 4h 50 min. The holder was directly mounted on the rotation stage PI U-651.

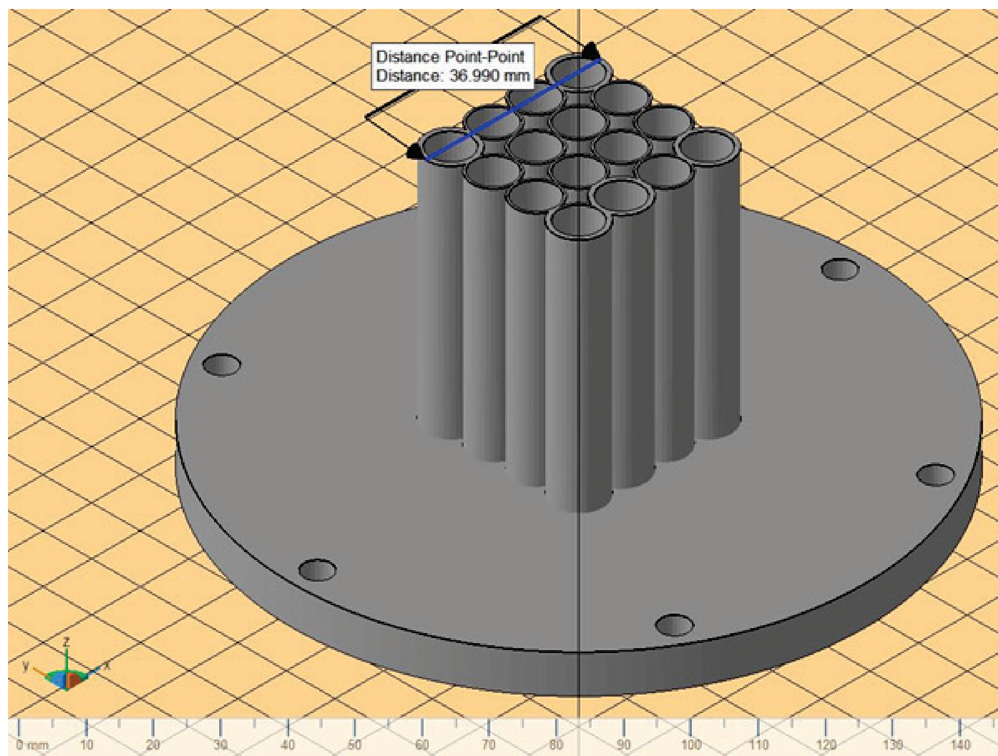

Figure S2: Model used for the 3D printing of the sample holder

S2. Generation of simulated Ni XRD-CT data

The normalised phantom intensity image used in this work is shown on the top left part of Figure S3. This image was segmented and each catalyst particle labeled (top middle of Figure S3). The TOPAS software was used to simulate 36 Ni diffraction patterns (right of Figure S3), equal to the number of the segmented particles. The range of Ni parameters used for the simulated diffraction patterns were the following: 3.525 - 3.575 Å for the Ni lattice parameter and 2 - 25 nm for the Ni crystallite size. Each catalyst particle was associated with a diffraction pattern meaning corresponding to a specific Ni lattice parameter value and crystallite size (bottom left and bottom middle of Figure S3).

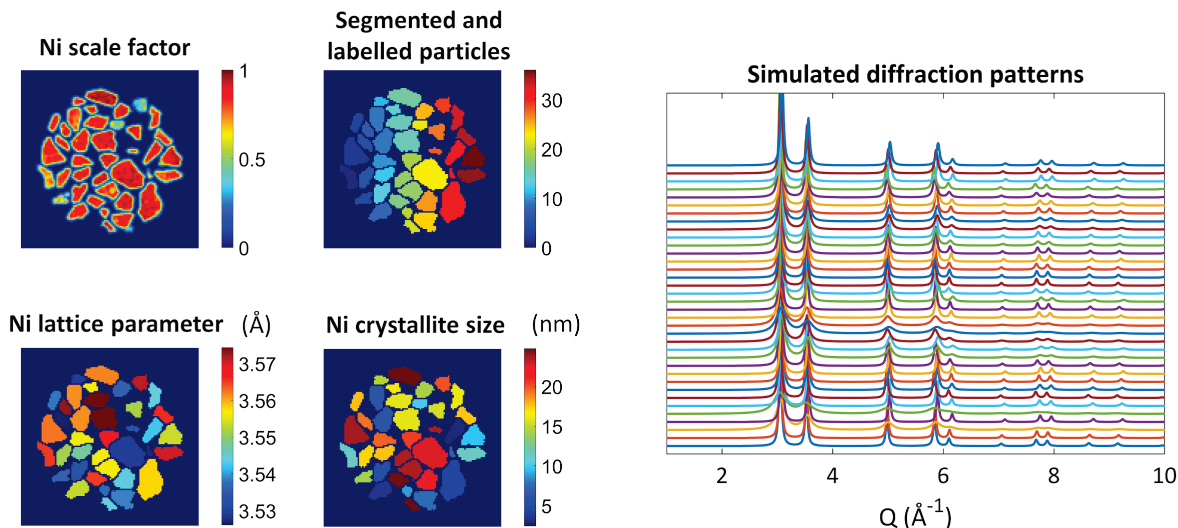

Figure S3: The intensity image (top left) was segmented to isolate the various catalyst particles which were then labeled (top middle). Each of the 36 simulated Ni diffraction patterns (right) were associated with a catalyst particle (bottom left and bottom middle).

S3. Performance of DLSR

In order to evaluate the performance of the DLSR method, multiple reconstruction tests using the Ni XRD-CT simulation data were performed and the results presented in Figure S4 and Table S1. It can be seen that the method is computationally memory expensive and beyond what can be achieved with present day's conventional office PCs.

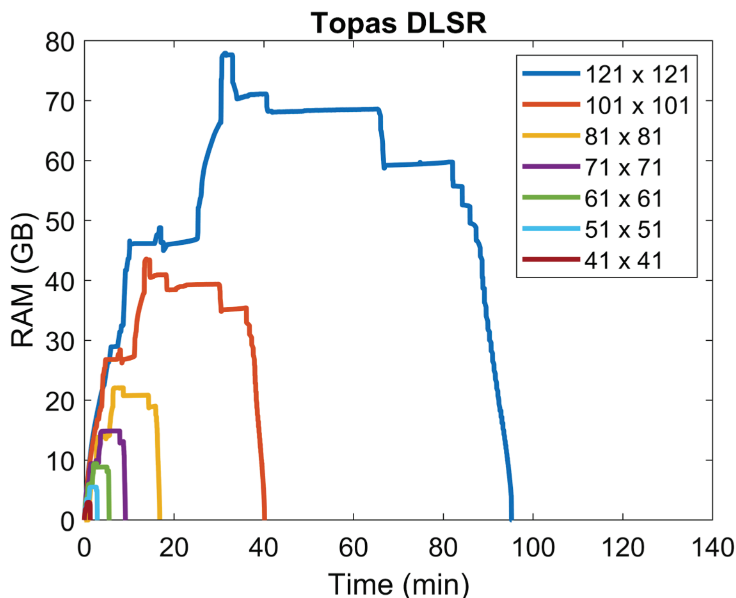

Figure S4: Memory requirements and time for convergence using the DLSR method for different size images.

Table S1: Performance of the DLSR method for different image sizes

Number of Patterns (nT × nA)	Number of Structure Models	TOPAS Rietveld Time (min)	Number of Iterations	Total TOPAS Time (min)	Max Memory (GB)
41 × 41	1681	1.2	34	1.3	2.9
51 × 51	2601	2.7	36	2.9	5.5
61 × 61	3721	5	39	5.5	9.4
71 × 71	5041	7.8	33	9.2	14.9
81 × 81	6561	13.4	38	16.8	22.1
101 × 101	10201	29.9	34	40.1	43.6
121 × 121	14641	65	37	95.2	77.9

S4. Impact of number of structure models

In an attempt to reduce the computational requirements for the DLSR method, a new approach was developed. Specifically, a binary mask was applied to mask out the region in the images which corresponds to void (i.e. non-sample containing regions). It can be seen that the new approach yields less noisy results and this can be attributed to a more stable refinement (i.e. a reduced number of refined parameters for the same number of patterns and observation points).

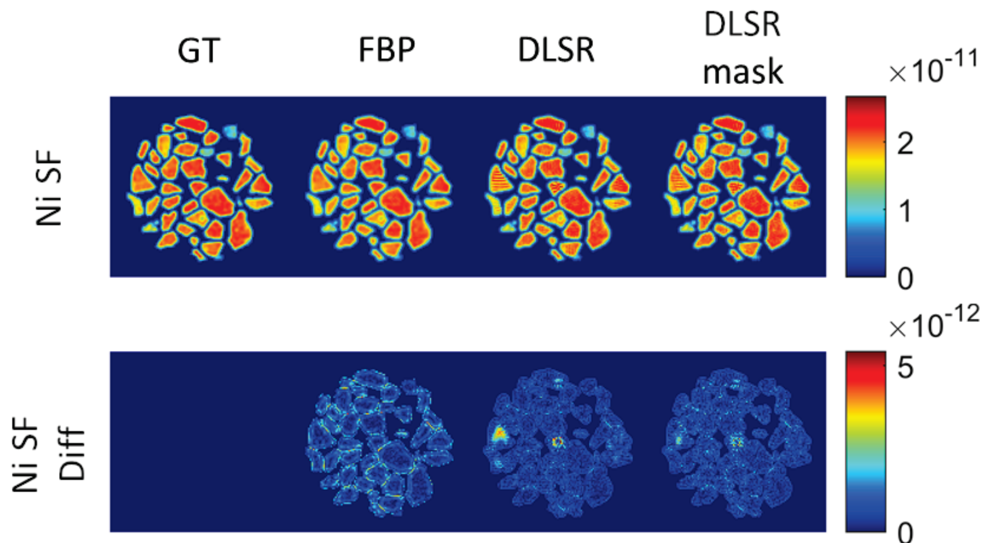

Figure S5: Top row: The normalised scale factor maps (ground truth and the ones obtained with three approaches), Bottom row: Absolute difference between the normalised scale factor maps obtained with three approaches and the ground truth map.

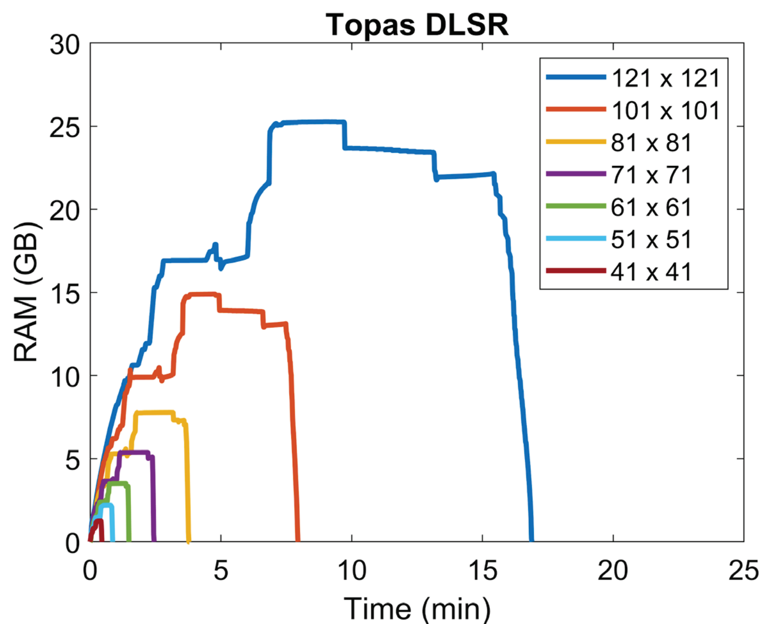

Figure S6: Memory requirements and time for convergence using the DLSR method for different size images using the mask approach.

Table S2: Performance of the DLSR method for different image sizes using the mask approach

Number of Patterns (nT × nA)	Number of Structure Models	TOPAS Rietveld Time (min)	Number of Iterations	Total TOPAS Time (min)	Max Memory (GB)
41 × 41	689	0.4	22	0.5	1.3
51 × 51	1007	0.8	23	0.9	2.2
61 × 61	1383	1.3	23	1.5	3.5
71 × 71	1828	2.2	24	2.4	5.4
81 × 81	2324	3.3	23	3.8	7.8
101 × 101	3499	6.6	21	7.9	14.9
121 × 121	5000	13.2	23	16.9	25.3

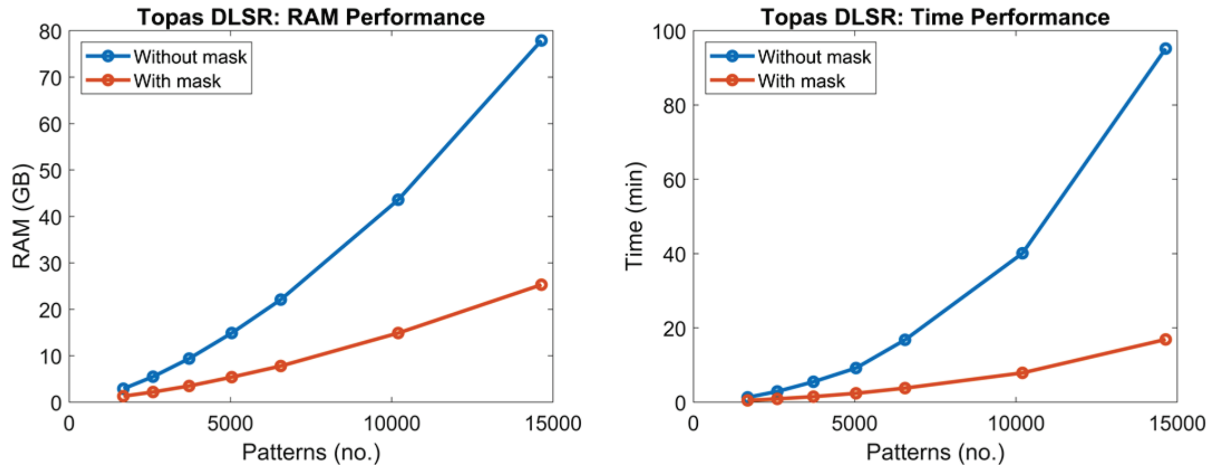

Figure S7: Memory requirements and time for convergence for different image sizes using the two DLSR approaches.

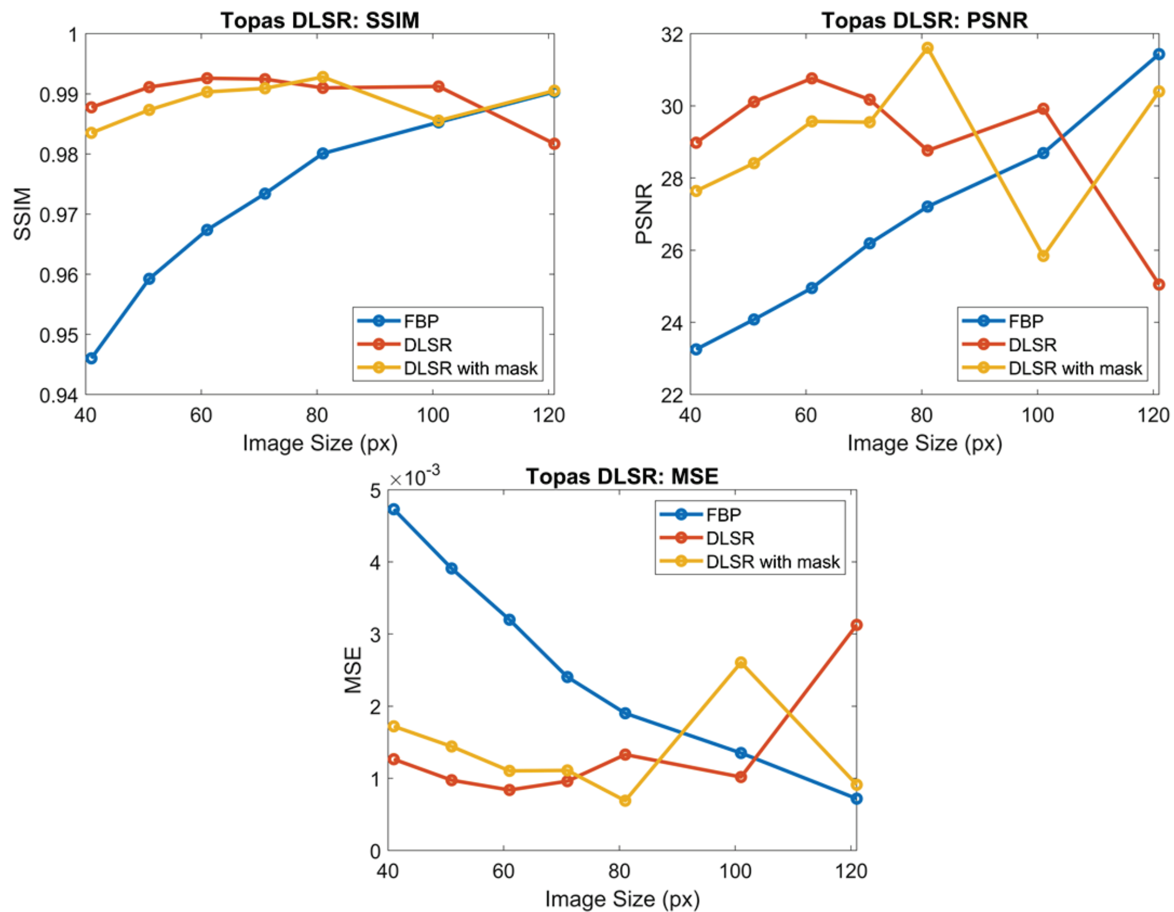

Figure S8: Comparison between the conventional and the two DLSR approaches for different image sizes using three metrics: structure similarity (SSIM), peak signal-to-noise ratio (PSNR) and mean-squared error (MSE)

S5. Impact of number of projections

The impact of the sinogram size was also investigated and the results are presented in Figures S9-10 and Table S3.

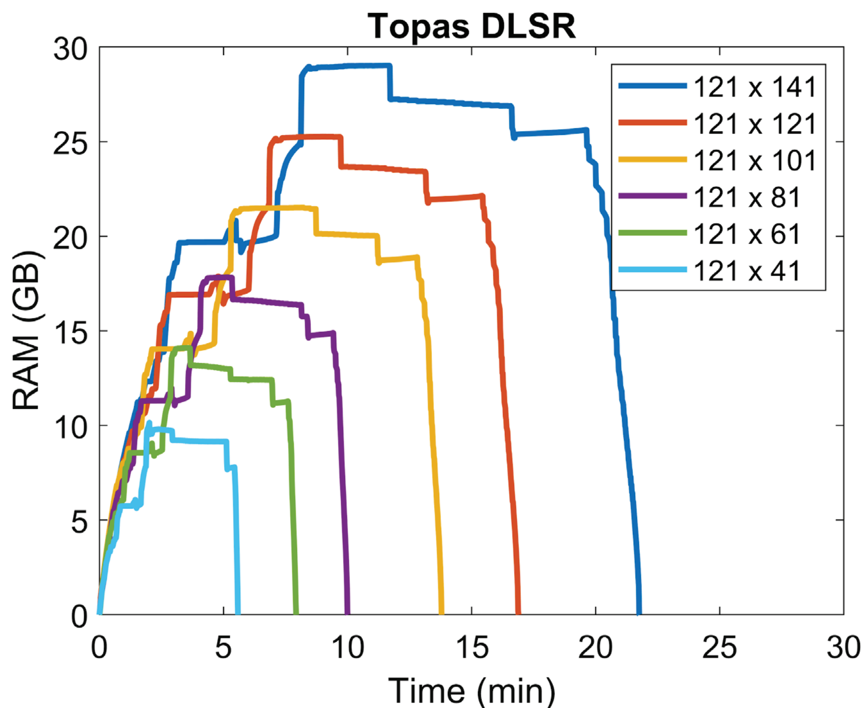

Figure S9: Memory requirements and time for convergence using the DLSR method for a 121 × 121 image size and various sinogram sizes using the mask approach

Table S3: Performance of the DLSR method for different sinogram sizes using the mask approach

Number of Patterns (nT × nA)	Number of Stucture Models	TOPAS Rietveld Time (min)	Number of Iterations	Total TOPAS Time (min)	Max Memory (GB)
121 × 41	5000	5.1	40	5.6	10.1
121 × 61	5000	6.9	34	7.9	14.1
121 × 81	5000	8.3	27	10.0	17.8
121 × 101	5000	11.1	27	13.8	21.5
121 × 121	5000	13.2	23	16.9	25.3
121 × 141	5000	16.5	25	21.8	29

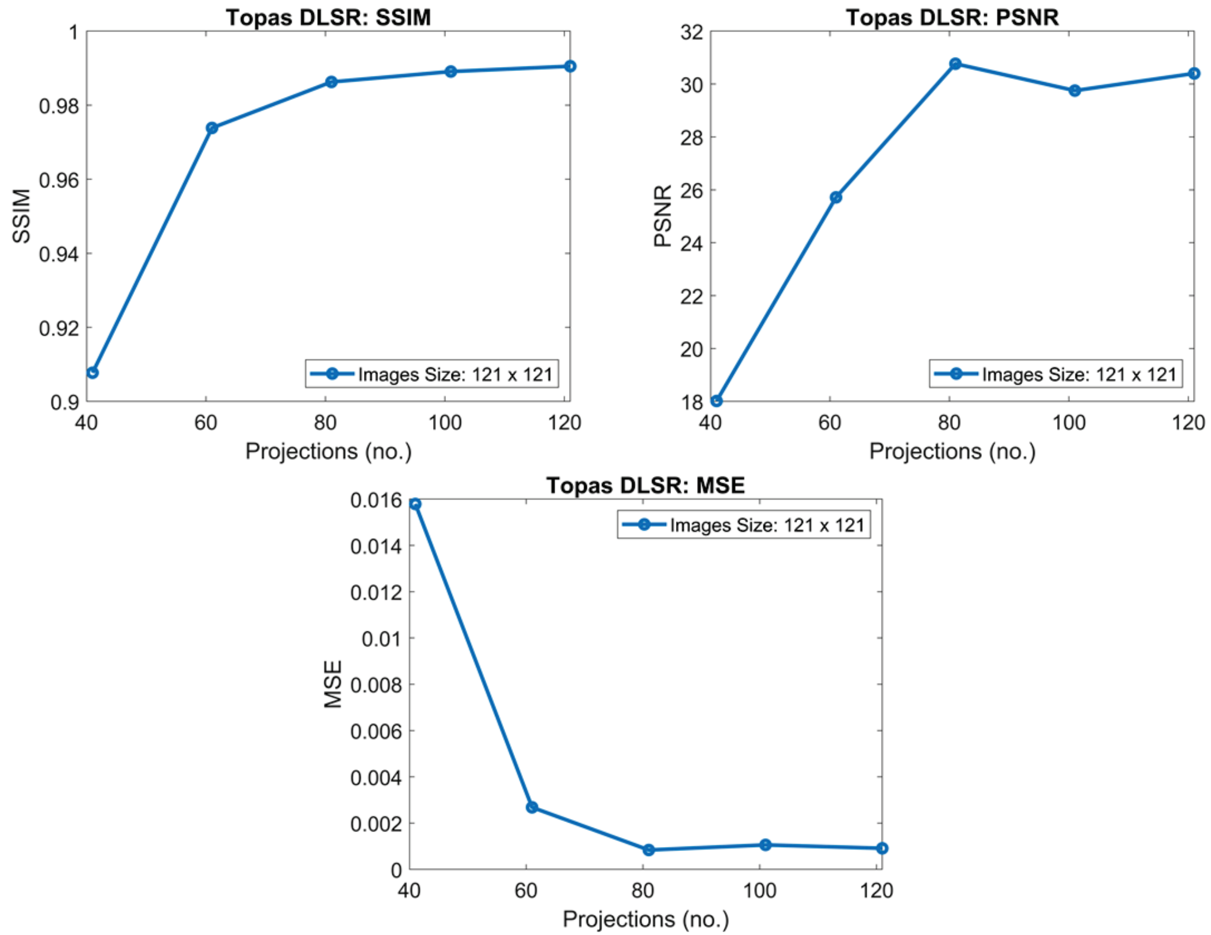

Figure S10: Impact of sinogram size on the quality of the DLSR reconstructed images using three metrics: structure similarity (SSIM), peak signal-to-noise ratio (PSNR) and mean-squared error (MSE)

S6. Impact of number of peaks/bins

The impact of the bin numbers (number of peaks) was also investigated and the results are presented in Figures S11-12 and Table S4.

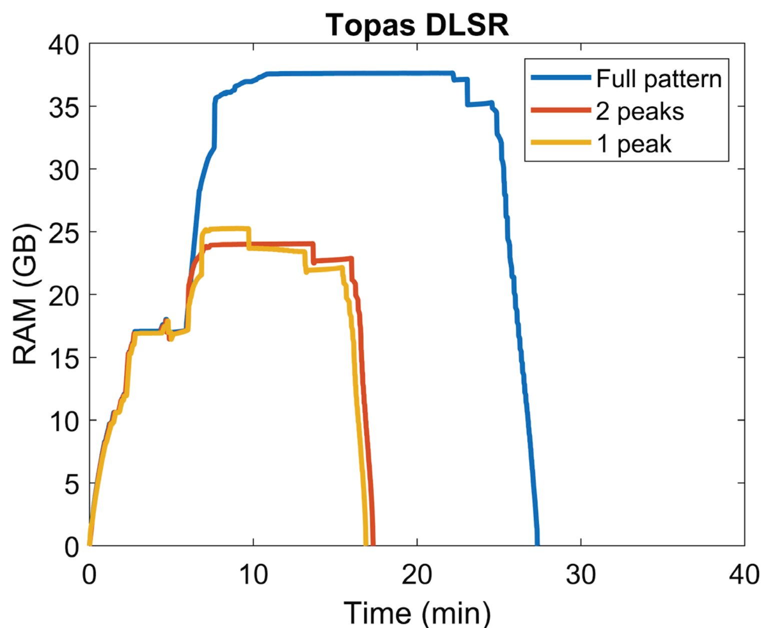

Figure S11: Memory requirements and time for convergence using the DLSR method for a 121 × 121 image size and various 121 × 121 × nB sinograms using the mask approach

Table S4: Performance of the DLSR method for different 121 × 121 × nB sinograms (3rd dimension is the diffraction dimension) using the mask approach

Number of observation points (nB)	Number of Reflections	TOPAS Rietveld Time (min)	Number of Iterations	Total TOPAS Time (min)	Max Memory (GB)
265	1	13.2	23	16.9	25.3
440	2	13.5	24	17.3	24
1450	9	22.5	24	27.9	37.6

In Figure S12, the ground truth maps are compared with the ones obtained with the DLSR approach using the mask for different numbers of peaks. As expected, due to the high symmetry of Ni (cubic space group), the addition of more peaks in the refinement process does not lead to significant improvements in the quality of the reconstructed images.

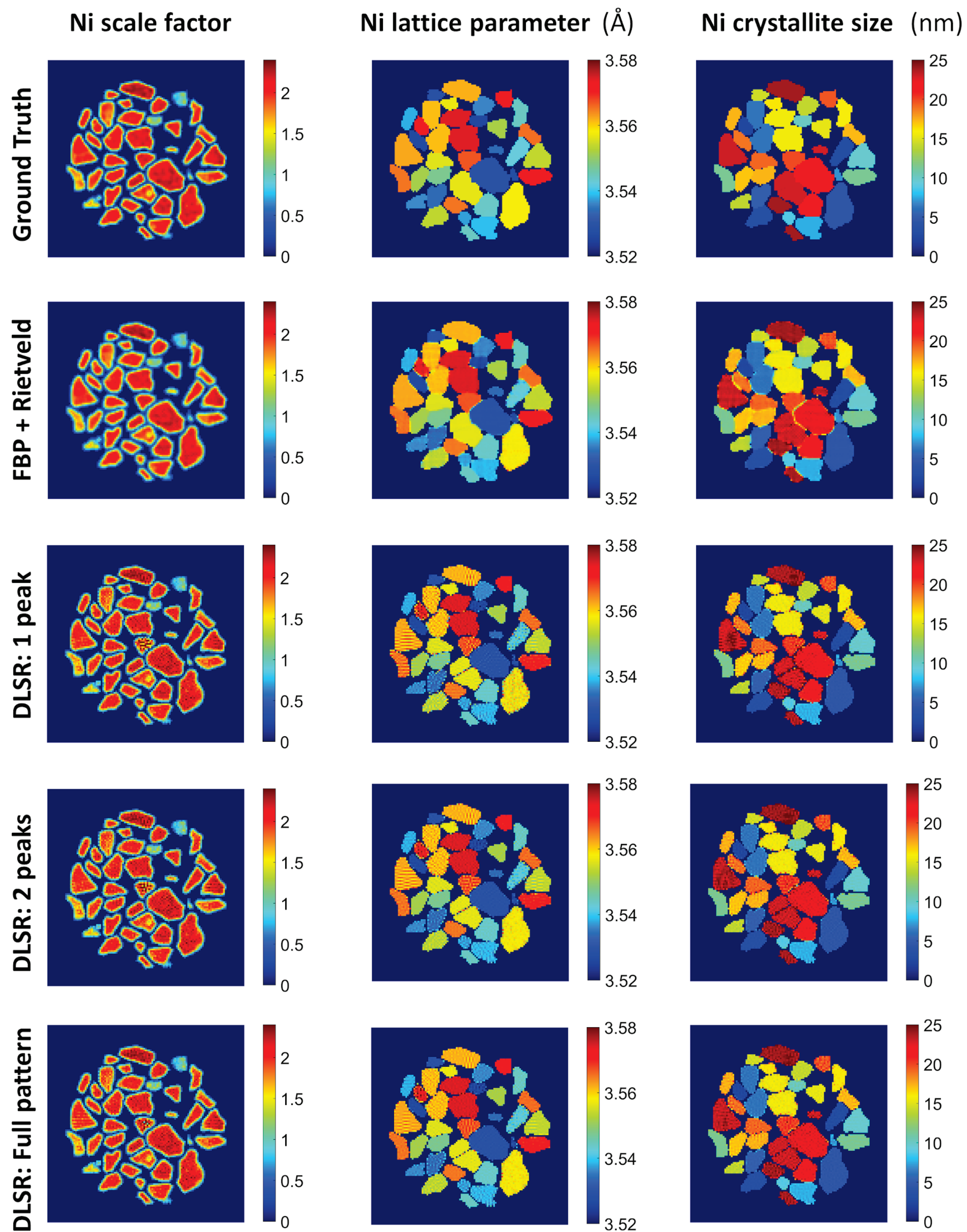

Figure S12: Comparison between the ground truth maps and the ones obtained with the DLSR approach using the mask for different numbers of peaks.

S7. Phase Identification

The results from the phase Identification are presented in Figure S13. All diffraction peaks are predicted by using the following three phases: TiO_2 rutile (ICSD: 33837 (Kazumasa Sugiyama & Yoshio Takéuchi, 1991)), MgO (ICSD: 9863 (SASAKI *et al.*, 1979)) and SiC (ICSD: 603798 (Li & Bradt, 1986)).

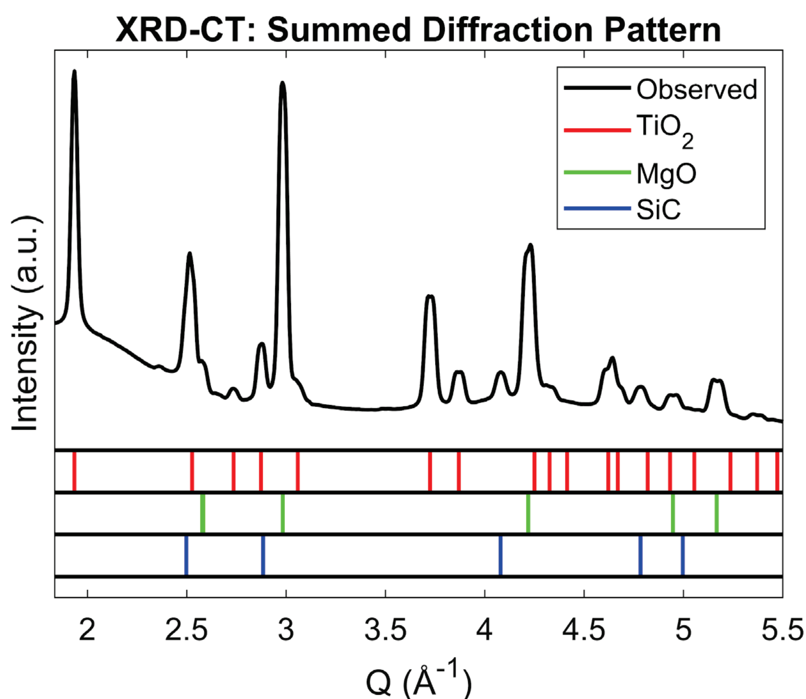

Figure S13: Phase identification using the summed XRD-CT diffraction pattern.

S8. Phantom XRD-CT patterns

The parallax artefact present in the experimental data from the 0-360° XRD-CT scan is demonstrated in Figure S14. In panel a, the global XRD-CT sinogram is presented while in panel b the mean diffraction patterns from every linescan acquired during the zigzag CT scan are shown. The peak splitting of the MgO phase is clearly visible (e.g. diffraction peak at ca. 4.2 $Å^{-1}$) showing that a single MgO structure model is not good enough to model the diffraction data. The position of the TiO_2 and SiC peaks as a function of tomographic angle is presented in panels c and d of Figure S14 respectively.

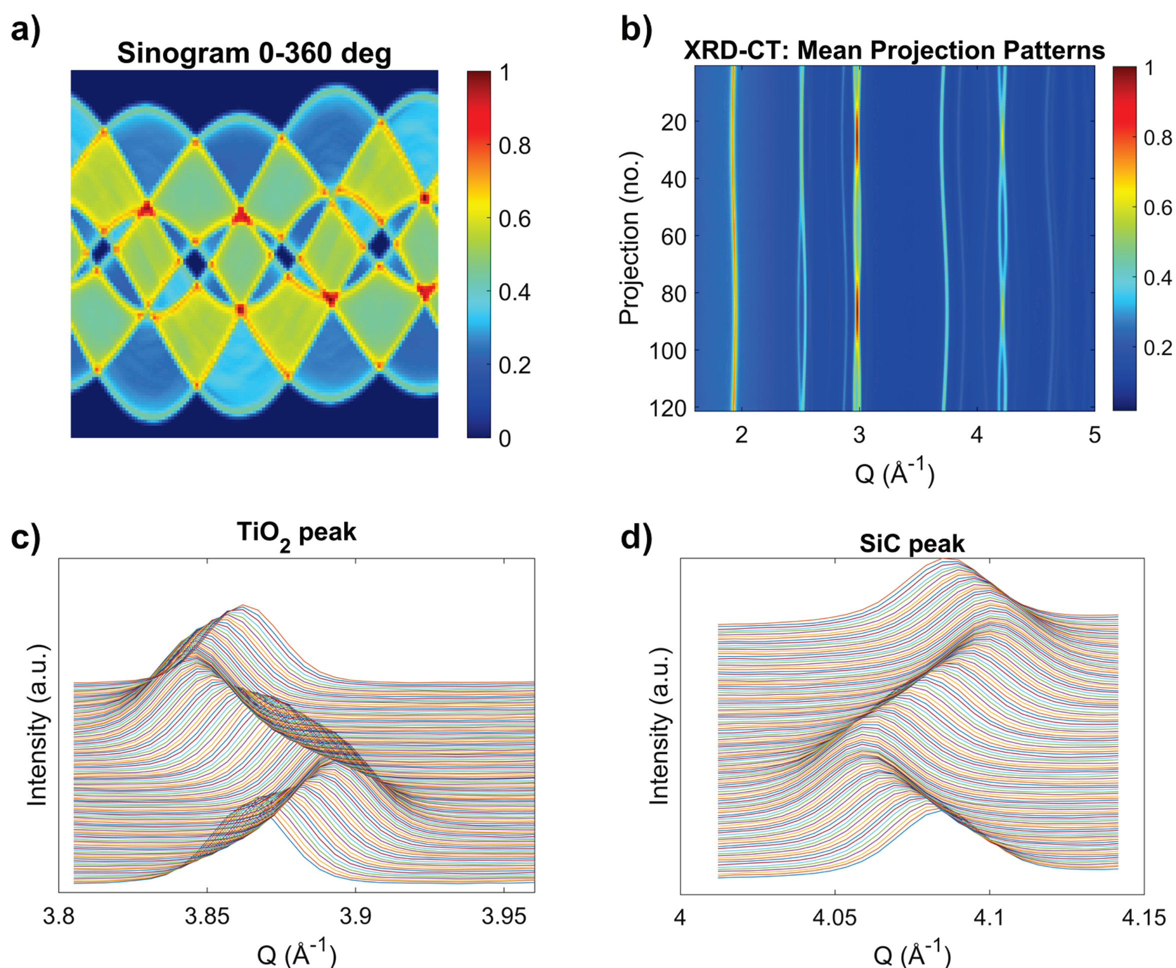

Figure S14: Parallax artefact present in XRD-CT data: a) Global XRD-CT sinogram from the 0-360° CT scan, b) Mean diffraction patterns per zigzag linescan, c) TiO_2 peak-of-interest position as derived from the mean diffraction pattern per zigzag linescan and d) SiC peak-of-interest position as derived from the mean diffraction pattern per zigzag linescan.

S9. Glass signal subtraction

For the subtraction of the glass signal, the following strategy was followed: (1) the glass phase distribution map was derived from the FBP reconstructed XRD-CT images (panel a in Figure S15), (2) a binary mask (panel b in Figure S15) was created based on the aforementioned glass image, (3) the binary mask was applied to the XRD-CT data volume to obtained a high quality glass pattern (panel c in Figure S15), (4) a synthetic XRD-CT dataset was created by combining the glass pattern and the glass distribution map (panel d in Figure S15), (5) this glass XRD-CT dataset was forward projected using the parallax projector to create a glass XRD-CT sinogram dataset containing parallax artefact (panel e in Figure S15). The latter was then subtracted from the raw XRD-CT sinogram data leading to a flat background in the diffraction patterns.

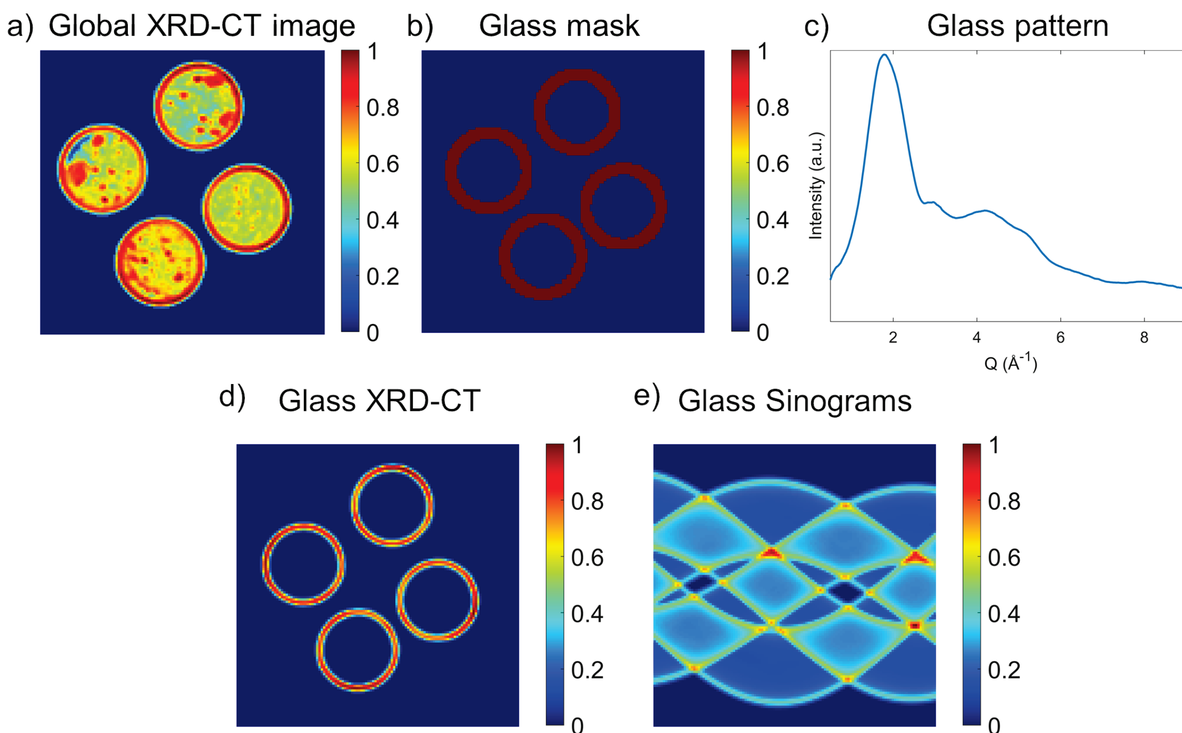

Figure S15: Glass subtraction process: a) FBP reconstructed XRD-CT images, b) Glass binary mask, c) Glass pattern, d) Synthetic glass XRD-CT real-space dataset, e) Glass XRD-CT sinograms containing parallax artefact.

S10. Detector calibration

An instrument parameter file was created from information derived from the full profile analysis of a CeO_2 diffraction data collected during the beamtime experiment. An 8th order Chebyshev polynomial was used to fit the background and a pseudo-Voigt profile function to fit the diffraction peaks. A CeO_2 CIF file was obtained from the ICSD database to be used for the Rietveld refinement (ICSD: 72155 (WoŁcyrz & Kepinski, 1992)). This instrument parameter file was then used for the Rietveld analysis of the XRD-CT data. As shown in Figure S16, the fit is very good (Rwp = 5.284 %).

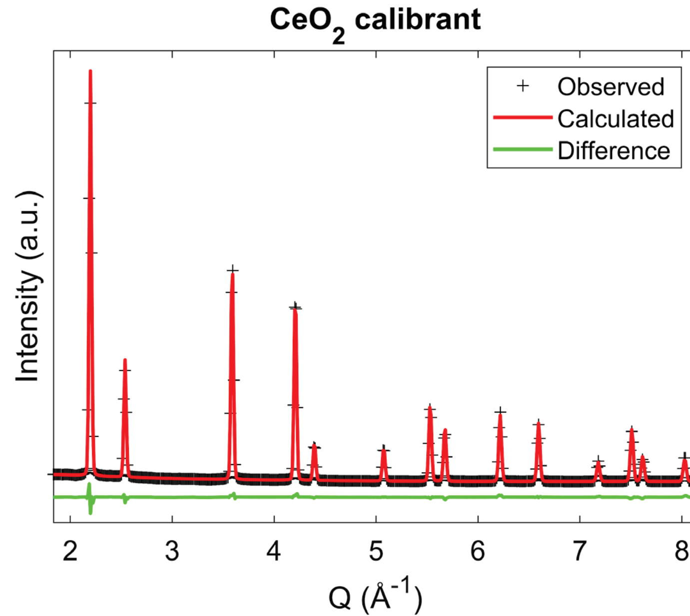

Figure S16: Full profile analysis of the diffraction pattern collected with a CeO2 standard during the beamtime experiment at beamline P07 of the DEST. Black: Observed pattern, Red: calculated pattern, Green: difference plot

S11. Rietveld analysis of a diffraction pattern of interest

The results from the full profile analysis of a diffraction pattern exported from the XRD-CT sinogram data after the glass signal subtraction are presented in Figures S17-18. Specifically, This pattern corresponds to the average of three patterns exported from the XRD-CT sinogram data. These patterns correspond to a TiO_2, a MgO and a SiC pattern. For the TiO_2 and SiC pattern, the sample orientation was the one shown on the left hand side of Figure S17 and the patterns were exported from the inner edge of the corresponding glass pipettes. This allows for the extraction of diffraction patterns that realistically represent the TiO_2 and SiC phases, minimising the parallax artefact (accurate diffraction peak shapes and positions). Similarly, for the MgO pattern another orientation was chosen where the MgO pipettes were orientated identically to the TiO_2 and SiC pipettes shown on the left hand side of Figure S17. Three structure models were used for the refinement, including the TiO_2, SiC and MgO phases. The parameters refined were the scale factors, lattice parameters and crystallite sizes of the four phases as well as the parameters of the shared pseudo-Voigt peak shape (global parameters shared between all phases). A 2nd degree Chebyshev polynomial was used to model the background. The results as shown in Figures S17-18 were of high quality, corresponding to Rwp 10.9 %.

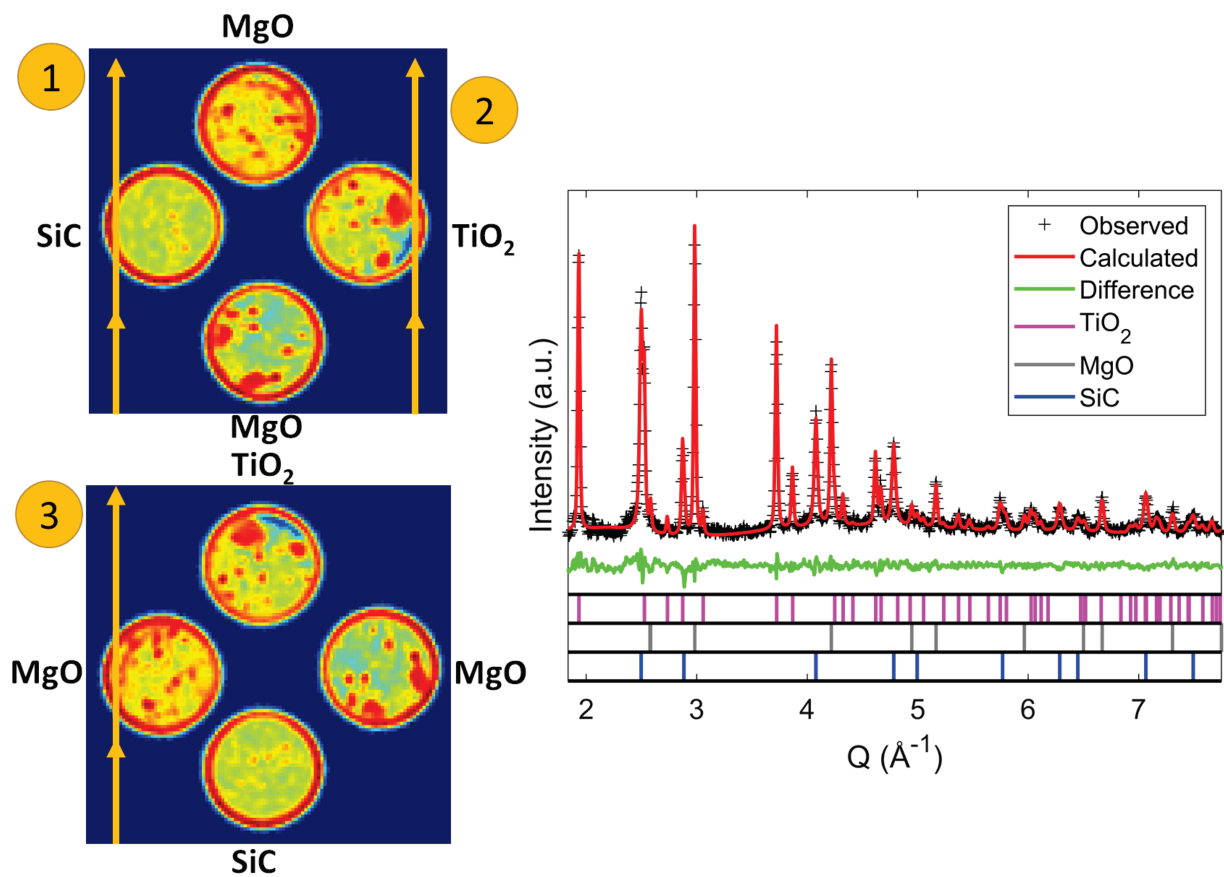

Figure S17: Left-top: Sample oriented at an angle where the SiC and TiO_2 phases were at the ideal sample-to-detector distance, Left-bottom: Sample oriented at an angle where the MgO phases were at the ideal sample-to-detector distance, Right: Rietveld analysis of a diffraction pattern exported from the sinogram XRD-CT data at these three positions (average pattern). Yellow arrows correspond to the translation positions (illustrating the X-ray beam).

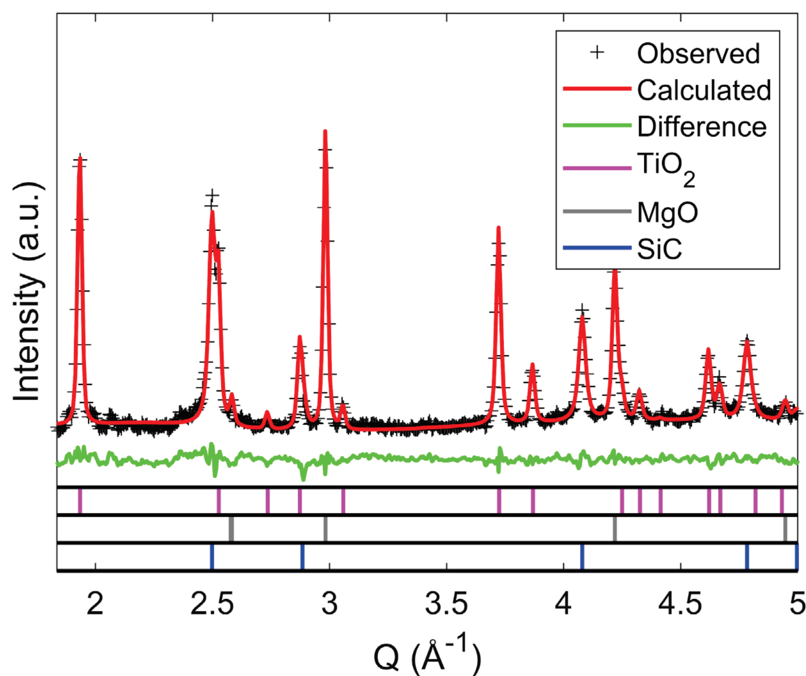

Figure S18: Magnified region-of-interest showing the quality of fit from the Rietveld analysis of the diffraction pattern shown in Figure S17

The values for the various parameters present in Table S5 serve as a means to assess the quality of the results obtained from the XRD-CT data analysis. It should be noted that the crystallite size values for the various phases obtained from XRD-CT data analysis should be greater than or equal to the ones shown in Table S5 (errors in brackets obtained from the Rietveld analysis with the TOPAS software).

Table S5: Results from the Rietveld analysis of diffraction pattern presented in Figures S17-18

	LPA (Å)	**LPC (Å)**	**CLS (nm)**
TiO_2	4.5963 (0.0002)	2.9589 (0.0002)	120 (10)
MgO	4.2128 (0.0001)	LPC = LPA	156 (17)
SiC	4.3566 (0.0002)	LPC = LPA	34 (2)

S12. Rietveld analysis of the phantom XRD-CT data

The results from the Rietveld analysis of the experimental XRD-CT data for both the 0-180° and 0-360° scans using the conventional and DLSR approaches are summarized in Table S6. For comparison, also presented are the results obtained from the region-of-interest diffraction pattern presented in Table S5. It should be noted that it is possible to apply soft restraints to the system of equations if the performance is unstable and/or there are undesired local outliers for the values of the various refined parameters (e.g. by setting the minimum and maximum value of a refined parameter to be between the average value of the nearest neighbors plus/minus a scalar or multiplied/divided by a scalar).

Table S6: Results from the Rietveld analysis of the experimental XRD-CT data. Values correspond to the round mean values obtained from the corresponding maps and in brackets is the round standard deviation.

		LPA (Å)	LPC (Å)	CLS (nm)
TiO_2	ROI sinogram	4.5963 (0.0002)	2.9589 (0.0002)	120 (10)
	FBP-180	4.6121 (0.0010)	2.9686 (0.0007)	53 (4)
	FBP-360	4.5931 (0.0003)	2.9560 (0.0013)	26 (3)
	DLSR-180	4.5931 (0.0001)	2.9570 (3.2E-5)	116 (2)
	DLSR-360	4.5932 (6E-5)	2.9570 (3.6E-5)	134 (2)
MgO	ROI sinogram	4.2128 (0.0001)	LPC = LPA	156 (17)
	FBP-180	4.2121 (0.0009)	LPC = LPA	61 (11)
	FBP-360	4.2117 (0.0005)	LPC = LPA	58 (24)
	DLSR-180	4.2118 (8.5E-5)	LPC = LPA	157 (3)
	DLSR-360	4.2118 (7.7E-5)	LPC = LPA	205 (3)
SiC	ROI sinogram	4.3566 (0.0002)	LPC = LPA	34 (2)
	FBP-180	4.3441 (0.0002)	LPC = LPA	27 (1)
	FBP-360	4.3585 (0.0001)	LPC = LPA	18 (1)
	DLSR-180	4.3580 (0.0001)	LPC = LPA	40 (1)
	DLSR-360	4.3580 (4E-5)	LPC = LPA	40 (1)